

FEDSM2026-184313

AN IN-SILICO INVESTIGATION OF RENAL ARTERY HEMODYNAMICS IN FENESTRATED ENDOVASCULAR ANEURYSM REPAIR USING THE LATTICE BOLTZMANN METHOD

Carter Groezinger, Arka Das, Leitao Chen

Department of Mechanical Engineering, Embry-Riddle Aeronautical University, Daytona Beach, FL, USA

ABSTRACT

Renal artery occlusion is a significant complication following fenestrated or branched endovascular aneurysm repair (F/B EVAR), often arising from adverse hemodynamic conditions induced by stent geometry and placement. Alterations in flow alignment, wall shear stress, and residence time within renal artery branches can promote thrombosis and compromise renal perfusion. Despite advances in endovascular stent design, the flow mechanisms governing post-operative occlusion remain incompletely understood.

In this study, patient-generic vascular models are employed to investigate the influence of branch stent tilt angle on renal artery hemodynamics. Two-dimensional flow simulations are performed using FluidX3D, a GPU-accelerated Lattice Boltzmann Method (LBM) solver capable of efficiently resolving complex vascular geometries. LBM-based simulations enable high-resolution analysis of velocity fields, vortex formation, and regions of low wall shear stress associated with thrombogenic risk.

Steady-state simulations are conducted to quantify flow disturbances introduced by geometric features of branch stents. Results demonstrate that reduced branch angle increase flow resistance and generate recirculation zones near the renal artery ostium, leading to prolonged particle residence time and diminished wall shear stress. These hemodynamic features are consistent with conditions known to promote thrombus initiation.

The findings highlight the utility of LBM-based computational modeling for evaluating vascular stent configurations and provide insights that may inform improved surgical planning and endovascular device design to reduce renal artery occlusion following F/B EVAR.

Keywords: Lattice Boltzmann Method; Computational Hemodynamics; Endovascular Aneurysm Repair; Renal Artery Flow

1. INTRODUCTION

Endovascular aneurysm repair (EVAR) has become the preferred treatment for infrarenal abdominal aortic aneurysms due to lower perioperative morbidity and mortality than open

repair [1]. However, standard EVAR is limited by the requirement for an adequate infrarenal neck, precluding its use in aneurysms extending to or involving the renal arteries. Fenestrated and branched endovascular aneurysm repair (F/B EVAR) was developed to address this limitation by enabling preservation of renal and visceral artery perfusion through fenestrations or directional branches incorporated into the main endograft [2–4]. These advanced techniques have demonstrated high technical success and acceptable mid- to long-term durability in appropriately selected patients [3,4].

Renal perfusion preservation remains a central determinant of procedural success in F/B EVAR. The kidneys receive approximately 20% of cardiac output, and renal blood flow is tightly regulated by autoregulatory mechanisms that maintain glomerular filtration across a range of perfusion pressures [5]. Even modest reductions in renal perfusion following aortic intervention are associated with deterioration in renal function, which is a strong independent predictor of long-term mortality [6]. Consequently, durable renal artery (RA) incorporation and branch patency are essential objectives in the endovascular treatment of complex abdominal and thoracoabdominal aortic aneurysms [5,6].

Despite technical advances, RA anatomy frequently limits the feasibility and durability of F/B EVAR. Comprehensive anatomic analyses have demonstrated that approximately one-fifth of patients present with absolute anatomic contraindications to renal artery incorporation, including small vessel diameter or early bifurcation, while an additional one-third exhibit challenging anatomy such as severe downward angulation, ostial stenosis, or prior renal stents [5]. Current device instructions for use typically recommend a minimum RA diameter of 4 mm and a length of at least 13 mm from the ostium to the first bifurcation to allow secure deployment and sealing of a bridging stent [5].

Failure to meet these criteria has been associated with increased procedural complexity and compromised branch patency.

Clinical outcome studies have confirmed that small renal artery targets are particularly vulnerable following F/B EVAR. Incorporation of RAs measuring less than 4 mm in diameter is associated with lower technical success, increased risk of arterial rupture, higher rates of branch instability, and significantly reduced primary and secondary patency at one year compared with larger renal arteries [8]. Although intentional coverage of small accessory renal arteries may be tolerated in selected patients, loss of a dominant renal artery or a substantial fraction of renal parenchyma is associated with ischemic injury and should be avoided whenever possible [5,7].

Beyond static anatomic suitability, branch stent geometry and deployment configuration play a critical role in determining post-operative hemodynamics. Fenestrated and branched stent grafts inherently alter flow patterns at the renal artery ostium due to protrusion of the bridging stent into the aortic lumen and redirection of inflow into the renal circulation [9,10]. Computational investigations have demonstrated that unfavorable branch angles and excessive protrusion depths lead to disturbed flow, low wall shear stress, and flow recirculation at the renal artery origin, conditions known to promote platelet aggregation and thrombus formation [9,10]. These hemodynamic disturbances provide a mechanistic explanation for clinically observed branch occlusion despite technically successful deployment.

Traditional imaging modalities, such as computed tomography angiography, provide detailed anatomical assessment but are inherently limited in their ability to resolve local flow fields and shear stress distributions. Computational modeling, therefore, represents a critical adjunct for elucidating the hemodynamic mechanisms underlying renal artery compromise following F/B EVAR. In this context, high-fidelity numerical approaches enable systematic evaluation of the influence of branch angle, protrusion depth, and flow conditions on renal artery perfusion, thereby informing strategies to optimize device design and deployment and reduce renal complications after complex endovascular repair.

In this study, we specifically aim to reproduce and interrogate the renal artery hemodynamic features reported by Wang et al. [6] using a lattice Boltzmann framework applied to a patient-generic geometry. By adopting comparable geometric configurations and flow conditions, the present work seeks to validate the ability of an LBM-based solver to capture key flow characteristics, including branch ostial recirculation, velocity redistribution, and angle-dependent flow separation. Establishing agreement with previously reported computational results provides a critical benchmark for assessing the fidelity and robustness of LBM in modeling post-F/B EVAR renal artery hemodynamics.

2. METHODOLOGY

2.1 Governing Equations and Lattice Boltzmann Formulation

Blood flow was simulated using the lattice Boltzmann method (LBM), a mesoscopic numerical approach derived from kinetic theory that solves for the evolution of particle distribution functions rather than directly discretizing the Navier-Stokes equations. In this work, the single-relaxation-time Bhantnagar Gross Krook (BGK) formulation was employed.

The discrete evolution equation for the particle distribution function f_i is given by:

$$f_i(x + c_i \Delta t, t + \Delta t) = f_i(x, t) - \frac{\Delta t}{\tau} (f_i(x, t) - f_i^{eq}(x, t)) \quad (1)$$

Where c_i are the discrete velocities, τ is the relaxation time, and f_i^{eq} is the equilibrium distribution function.

The relaxation time is related to the kinematic viscosity ν by:

$$\nu = c_s^2 (\tau - 0.5) \Delta t \quad (2)$$

Where c_s is the D2Q9 speed of sound, or $c_s = \frac{1}{\sqrt{3}}$.

LBM has been extensively validated for hemodynamic applications and has demonstrated strong agreement with Navier-Stokes-based solvers for arterial flow [11]. Its ability to accurately capture flow separation and recirculation has led to increasing adoption [12].

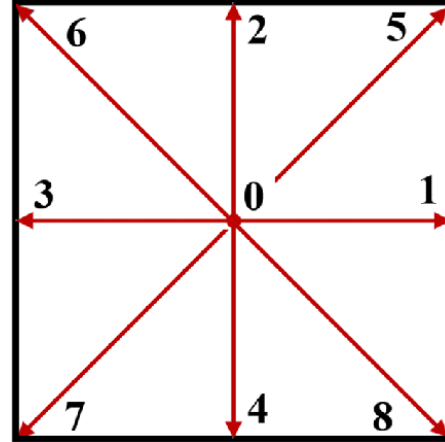


FIGURE 1: SCHEMATIC OF LBM LATTICE AND DISCRETE VELOCITY DIRECTIONS, D2Q9 LATTICE

2.2 Numerical Implementation Using FluidX3D

All simulations were performed using FluidX3D, a highly optimized, open-source LBM solver developed by Dr. Moritz Lehmann [13]. FluidX3D is designed specifically for GPU acceleration, enabling efficient simulation of large three-dimensional domains with minimal computational overhead.

Unlike conventional CFD solvers that require complex mesh generation and matrix assembly, FluidX3D uses a structured lattice and local update rules, resulting in near-linear

scaling with problem size. Previous studies have shown that GPU-accelerated LBM implementations can achieve orders of magnitude speedups compared to CPU-based solvers while maintaining numerical accuracy [14].

This computational efficiency is critical for the present study, as the Reynolds numbers relevant to renal artery flow following F/B EVAR need an extremely fine mesh resolution resulting in long simulation times, motivating the transition to a GPU accelerated solver like FluidX3D.[15].

Number of node	Consumed time of CPU-MOC (s)	Consumed time of GPU-LBM (s)	Speedup ratio
4507	14.62	1.69	8.7
36,053	119.44	3.25	36.7
180,261	515.93	8.52	60.5

FIGURE 2: THE AVERAGE CONSUMED TIME AND SPEEDUP RATIO OF GPU-LBM AND CPU-METHOD OF CHARACTERISTICS

2.3 Patient-Generic Vascular Model Construction

A patient-generic vascular geometry was constructed to replicate the theoretical model described by Wang et al. [9]. The geometry consists of a straight aortic segment with a single branch representing a renal artery stent.

The aorta was modeled as a channel-like, two-dimensional conduit with diameter D_1 , while the branch stent was represented as a cylindrical conduit of diameter D_2 , oriented at a prescribed tilt angle θ relative to the aortic axis. Consistent with the parametric definitions used in Wang et al. [9].

The use of patient-generic models is well established in vascular modeling, particularly when the objective is to isolate the influence of geometric parameters such as tilt angle [16]. This approach allows for systematic exploration of hemodynamic trends without the confounding variability introduced by patient-specific geometries.

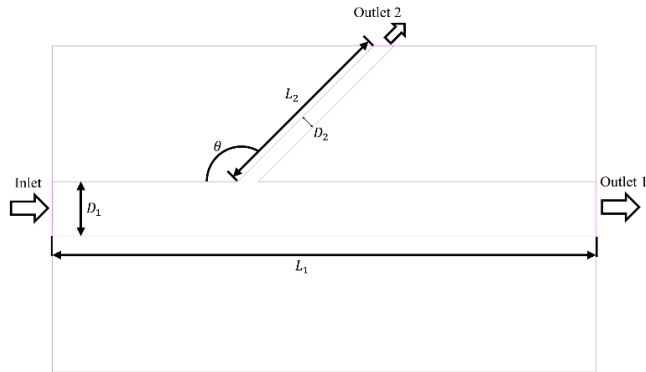


FIGURE 3: GEOMETRY SCHEMATIC SHOWING D_1, D_2 , and θ

2.4 Boundary Conditions and Flow Driving Mechanisms

Flow within the aorta was driven by pressure (density) based boundary conditions. At all three boundaries, a constant

prescribed density was applied, allowing pressure-driven flow partitioning between the aortic and branch outlets.

All vessel walls were treated as no-slip boundaries, enforcing zero velocity at the solid-fluid interface. This assumption is standard in hemodynamic simulations and has been shown to adequately capture wall shear stress and near-wall flow behavior in comparable studies [11].

2.5 Simulation Parameters and Post-Processing

Simulations were performed until steady-state conditions were achieved, as determined by convergence of velocity and flow rate metrics. Flow fields were exported in VTK format and analyzed using ParaView. Velocity magnitude contours, vector plots, and streamline visualizations were generated to identify regions of flow separation and recirculation.

These metrics have been shown to correlate strongly with thrombus formation and arterial occlusion risk in renal arteries following F/B EVAR [9].

3. RESULTS AND DISCUSSION

3.1 Flow Field Characteristics in the Patient-Generic Model

Steady-state simulations were performed for the patient-generic renal artery model under uniform inlet velocity conditions corresponding to the physiological Reynolds number reported in prior studies. Flow was driven through the aorta with a constant entry density. All results presented correspond to fully developed flow after transient effects had dissolved.

Figure 4 illustrates the velocity magnitude field within the aorta-branch configuration for a branch angle of $\theta = 45^\circ$. Higher-velocity flow is observed along the centerline of the main aorta, with a gradual velocity decay toward the vessel walls due to no-slip boundary conditions. Flow entering the branch exhibits a distinct acceleration region adjacent to a substantial recirculation.

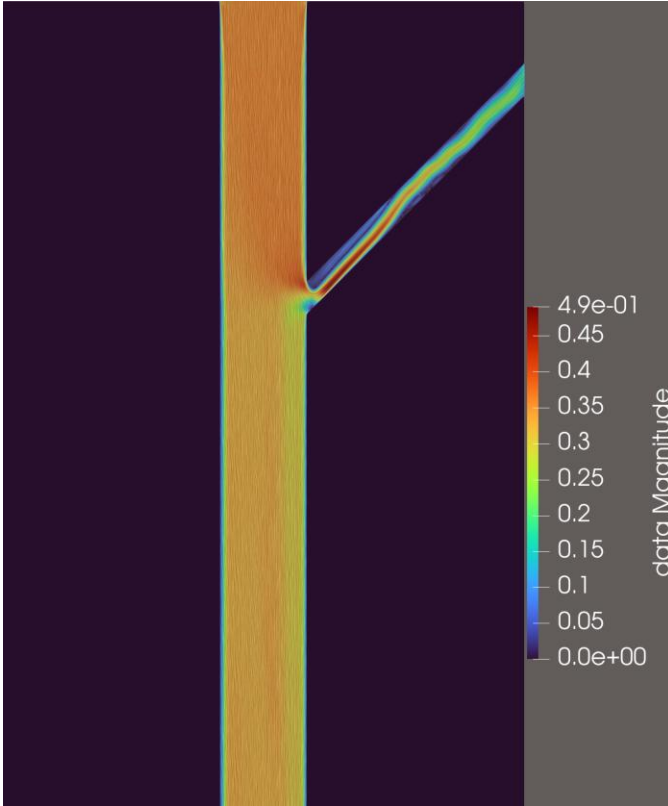


FIGURE 4: VELOCITY VECTOR PLOT FOR $\theta = 45^\circ$

3.2 Recirculation and Flow Separation Near the Branch Ostium

Velocity vector and streamline visualizations reveal localized recirculation zones near the branch ostium, particularly along the downstream wall of the branch entrance. These regions are characterized by low-magnitude velocities and reversed flow direction relative to the main aortic stream.

Figure 5 highlights this behavior through velocity vector plots overlaid on velocity magnitude contours. A separation bubble forms immediately downstream of the branch entry, consistent with flow misalignment induced by the branch angle. The location and extent of this recirculation zone closely match those reported in the reference study, indicating that the present model captures the essential hemodynamic features associated with angled branch stent deployment.

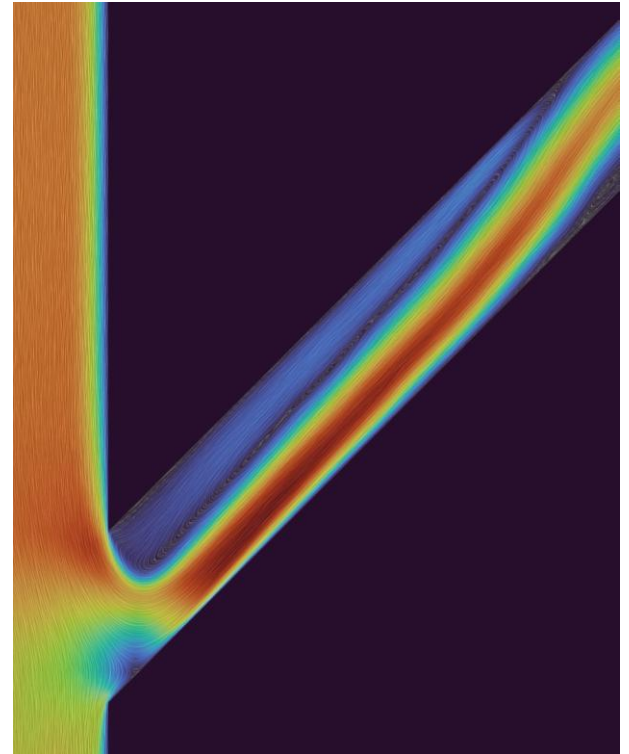


FIGURE 5: VELOCITY VECTOR PLOT OF THE BRANCH OSTIUM REGION, HIGHLIGHTING RECIRCULATION

3.3 Effect of Branch Angle on Local Hemodynamics

Simulations were repeated for multiple branch angles to assess the sensitivity of local hemodynamics to stent orientation. As the branch angle increased, a corresponding decrease in flow separation was observed at the branch entrance. Smaller angles led to expanded low-velocity regions adjacent to the branch wall.

These trends are consistent with previously reported findings, which associate decreased branch angle with elevated residence time near the ostium. The present results demonstrate that the Lattice Boltzmann framework implemented in FluidX3D can resolve these angle-dependent flow features without requiring turbulence modeling or mesh refinement.

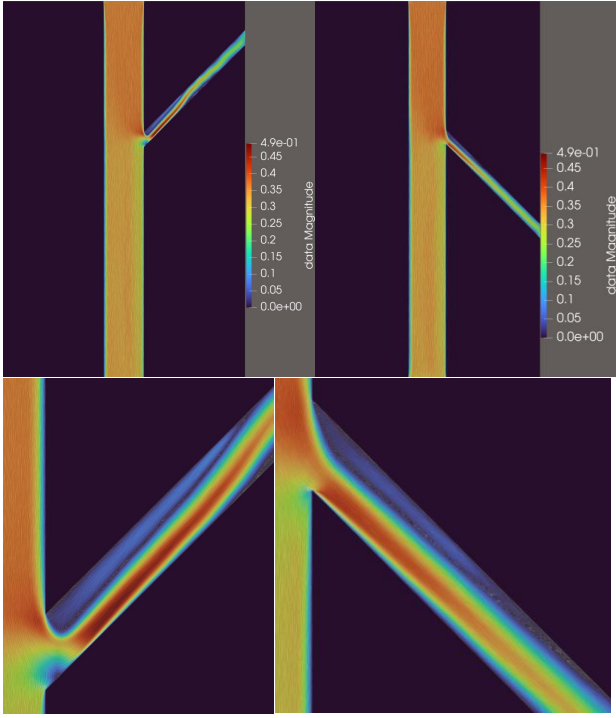


FIGURE 6: COMPARISON OF VELOCITY MAGNITUDE PLOT FOR $\theta = 45$ and $\theta = 135$

3.4 Comparison with Published Computational Results

Qualitative comparison between the present simulations and published computational results shows a strong agreement in both global and local flow patterns. In particular, the location of recirculation zones, velocity acceleration within the branch, and overall flow partitioning between the aorta and branch closely resemble those reported in the reference study Wang et al. [9].

Minor discrepancies in velocity magnitude near the branch outlet are attributed to differences in boundary condition formulation. Despite this, the overall agreement supports the validity of the patient-generic model and demonstrates the suitability of LBM for vascular hemodynamic studies.

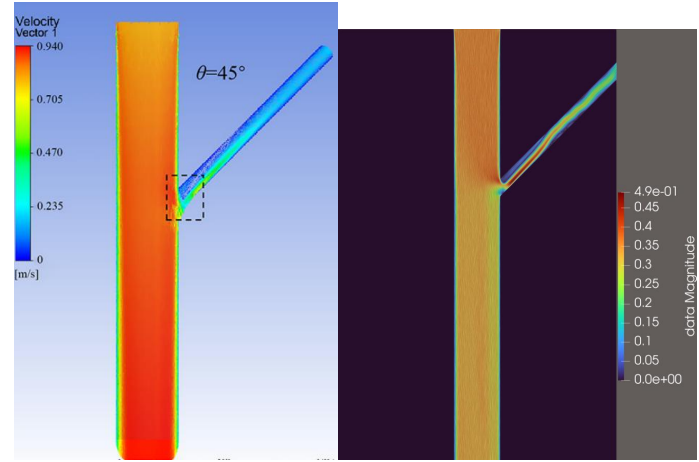


FIGURE 7: COMPARISON OF REFERENCE VELOCITY PLOT TO FLUIDX3D PLOT AT $\theta = 45^\circ$

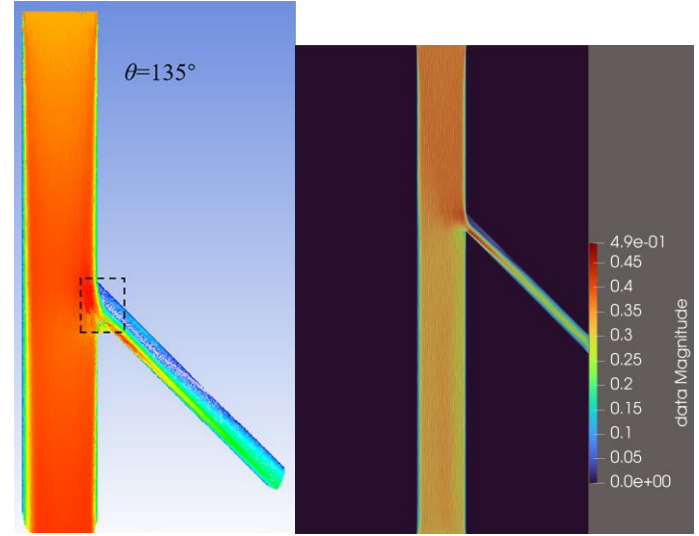


FIGURE 8: COMPARISON OF REFERENCE VELOCITY PLOT TO FLUIDX3D PLOT AT $\theta = 135^\circ$

3.5 Computational Performance

All simulations were executed on a GPU-accelerated platform using FluidX3D. The solver achieved steady-state convergence within a practical computational time frame, enabling high-resolution studies at a drastically lower computational cost when compared to traditional Navier-Stokes solvers. The efficiency of the Lattice Boltzmann Method, combined with GPU acceleration, allows for rapid evaluation of multiple stent configurations, supporting its use in design optimization and surgical recommendation.

4. CONCLUSION

This study demonstrates that a GPU-accelerated lattice Boltzmann framework can reliably capture key hemodynamic features associated with renal artery branch stents following fenestrated endovascular aneurysm repair. Using a patient-generic model, the simulations reproduced flow separation, recirculation zones, and branch angle-dependent trends that are

consistent with previously published computational investigations [9]. The observed agreement supports the validity of LBM as a high-fidelity alternative to conventional Navier–Stokes solvers for vascular hemodynamics in complex stented geometries.

Importantly, the computational efficiency afforded by GPU-based LBM enables rapid parametric evaluation of stent configurations, making it well suited for exploratory studies aimed at understanding adverse flow environments associated with renal artery occlusion. As such, the present work highlights the potential of LBM-based modeling as a valuable tool for device evaluation and procedural planning in fenestrated and branched endovascular aneurysm repair. Future extensions to three-dimensional, pulsatile, and non-Newtonian flow simulations will further enhance the physiological relevance of this approach.

REFERENCES

- [1] Parodi, J. C., Palmaz, J. C., & Barone, H. D. (1991). Transfemoral intraluminal graft implantation for abdominal aortic aneurysms. *Annals of vascular surgery*, 5(6), 491-499.
- [2] Mendes, B. C., Oderich, G. S., De Souza, L. R., Banga, P., Macedo, T. A., DeMartino, R. R., ... & Gloviczki, P. (2016). Implications of renal artery anatomy for endovascular repair using fenestrated, branched, or parallel stent graft techniques. *Journal of vascular surgery*, 63(5), 1163-1169.
- [3] Greenberg, R. K., Sternbergh III, W. C., Makaroun, M., Ohki, T., Chuter, T., Bharadwaj, P., ... & Fenestrated Investigators. (2009). Intermediate results of a United States multicenter trial of fenestrated endograft repair for juxtarenal abdominal aortic aneurysms. *Journal of vascular surgery*, 50(4), 730-737.
- [4] Oderich, G. S., Ribeiro, M., de Souza, L. R., Hofer, J., Wigham, J., & Cha, S. (2017). Endovascular repair of thoracoabdominal aortic aneurysms using fenestrated and branched endografts. *The Journal of thoracic and cardiovascular surgery*, 153(2), S32-S41.
- [5] Mendes, B. C., Oderich, G. S., De Souza, L. R., Banga, P., Macedo, T. A., DeMartino, R. R., ... & Gloviczki, P. (2016). Implications of renal artery anatomy for endovascular repair using fenestrated, branched, or parallel stent graft techniques. *Journal of vascular surgery*, 63(5), 1163-1169.
- [6] Zarkowsky DS, Hicks CW, Bostock IC, Stone DH, Eslami M, Goodney PP. Renal dysfunction and the associated decrease in survival after elective endovascular aneurysm repair. *J Vasc Surg*. 2016 Nov;64(5):1278-1285.e1. doi: 10.1016/j.jvs.2016.04.009. Epub 2016 Jul 29. PMID: 27478004; PMCID: PMC5079759.
- [7] Karmacharya, J., Parmer, S. S., Antezana, J. N., Fairman, R. M., Woo, E. Y., Velazquez, O. C., ... & Carpenter, J. P. (2006). Outcomes of accessory renal artery occlusion during endovascular aneurysm repair. *Journal of vascular surgery*, 43(1), 8-13.
- [8] Kärkkäinen, J. M., Tenorio, E. R., Pather, K., Mendes, B. C., Macedo, T. A., Wigham, J., ... & Oderich, G. S. (2020). Outcomes of small renal artery targets in patients treated by fenestrated-branched endovascular aortic repair. *European Journal of Vascular and Endovascular Surgery*, 59(6), 910-917.
- [9] Wang, Y., Sang, Y., Li, W., Zhou, M., Zhao, Y., He, X., ... & Liu, Z. (2025). A Computational Study on Renal Artery Anatomy in Patients Treated with Fenestrated or Branched Endovascular Aneurysm Repair. *Bioengineering*, 12(5), 482.
- [10] Sengupta, S., Zhu, Y., Hamady, M., & Xu, X. Y. (2022). Evaluating the haemodynamic performance of endografts for complex aortic arch repair. *Bioengineering*, 9(10), 573.
- [11] Zavodszky, G., 2015, *Hemodynamic Investigation of Arteries Using the Lattice Boltzmann Method*, Ph.D. thesis, Budapest University of Technology and Economics, Budapest, Hungary.
- [12] Yu, H., Khan, M., Wu, H., Zhang, C., Du, X., Chen, R., Fang, X., Long, J., and Sawchuk, A. P., 2022, "Inlet and Outlet Boundary Conditions and Uncertainty Quantification in Volumetric Lattice Boltzmann Method for Image-Based Computational Hemodynamics," *Fluids*, 7(1), p. 30. <https://doi.org/10.3390/fluids7010030>
- [13] Lehmann, M., 2022, FluidX3D, GitHub repository, <https://github/ProjectPhysX/FluidX3D> (accessed January 26, 2026)
- [14] Esfahani, S. S., Zhai, X., Chen, M., Amira, A., Bensaali, F., AbiNahed, J., Dakua, S., Younes, G., Baobeid, A., Richardson, R. A., and Coveney, P. V., 2020, "Lattice-Boltzmann Interactive Blood Flow Simulation Pipeline," *Int. J. Comput. Assist. Radiol. Surg.*, 15(4), pp. 629–639.
- [15] Meng, W., Yang, S., Lu, X., Peng, Y., Diao, W., and Zhang, C., 2025, "Lattice Boltzmann Model and Its GPU Acceleration for Transient Flow in Channel and Pressurized Pipe Combined Water Delivery System," *Applied Water Science*, 15(60). <https://doi.org/10.1007/s13201-025-02400-w>
- [16] Hamidah, M. A., and Hossain, S. M. C., 2024, "Modeling Analysis of Pulsatile Non-Newtonian Blood Flow in a Renal Bifurcated Artery With Stenosis," *International Journal of Thermofluids*, 22, p. 100645.